Plane mixing layer vortical structure kinematics

By R. L. LeBoeuf

The objective of the current project was to experimentally investigate the structure and dynamics of the streamwise vorticity in a plane mixing layer. The first part of this research program was intended to clarify whether the observed decrease in mean streamwise vorticity in the far-field of mixing layers (Bell & Mehta 1992) is due primarily to the "smearing" caused by vortex meander or to diffusion. Two-point velocity correlation measurements have been used to show that there is little spanwise meander of the large-scale streamwise vortical structure. The correlation measurements also indicate a large degree of transverse meander of the streamwise vorticity which is not surprising since the streamwise vorticity exists in the inclined braid region between the spanwise vortex core regions. The streamwise convection of the braid region thereby introduces an apparent transverse meander into measurements using stationary probes. These results were corroborated with estimated secondary velocity profiles in which the streamwise vorticity produces a signature which was tracked in time.

1. Motivation and objectives

An extensive data set consisting of single-point mean and turbulence statistics has been obtained for a two-stream mixing layer (Bell & Mehta 1989b, 1992). The plane unforced mixing layer originating from laminar boundary layers was examined in order to quantify the development of streamwise vorticity which previously was identified only through flow visualization studies (e.g. Bernal & Roshko, 1986). The mean streamwise vorticity derived from the mean velocity field shows a continuous decrease in magnitude with streamwise distance from its nearfield occurrence. It is unclear whether the decrease in mean vorticity is a result of diffusion of the streamwise vorticity or due to meander of concentrated vorticity. Based on comparisons with forced streamwise vortex meander in a boundary layer, Bell & Mehta (1992) argued that the observed decrease of the mean vorticity in the far-field mixing layer was more likely a result of diffusion.

Townsend (1976) showed that the governing equations for a free-shear flow admit to self-preserving solutions for sufficiently high Reynolds numbers. The resulting "self-similar" mean and Reynolds stress profiles become functions of single length and velocity scales. Previous measurements (Bell & Mehta 1992) have indicated that the streamwise vorticity persists even in what would normally be considered the "self-similar" region (where a linear mixing layer growth rate and asymptotic peak Reynolds stresses were achieved). The peak streamwise vorticity and the secondary shear stress ($\overline{uw}$), which was strongly correlated with the streamwise vorticity, were found to exhibit significant levels in this region (although they decreased with streamwise distance to levels comparable with the noise threshold). It

is important for the establishment of the criteria for "self-similarity" to investigate whether the measured decay is due to true diffusion of the streamwise vorticity or an artifact of meander. In addition, this assessment will have important implications regarding the ability of the layer to enhance mixing and reaction rates in the far-field.

To resolve the questions regarding the persistence of streamwise vorticity in the far-field, it was proposed to perform two-point cross-wire measurements of the velocity field (Bell 1990). The dependence of the velocity cross-correlation on the fixed probe location is considered a good indicator of the stationarity of the streamwise vortex location. Additional information regarding meander can be obtained from instantaneous velocity profiles. These were estimated using a newly developed technique and the current apparatus (LeBoeuf & Mehta 1992). The facility and flow conditions that were used for the current study are similar to those of Bell & Mehta (1992).

2. Accomplishments

2.1 Experiment and apparatus

The experiments were conducted in a *Mixing Layer Wind Tunnel* specifically designed for free-shear flow experiments (Bell & Mehta 1989b). The wind tunnel consists of two separate legs which are driven independently by centrifugal blowers connected to variable speed motors. The two streams merge at the sharp trailing edge of a slowly tapering splitter plate; the included angle at the splitter plate edge, which extends 15 cm into the test section, is about 1°. The test section is 36 cm in the cross-stream direction, 91 cm in the spanwise direction, and 366 cm in length. One side-wall is adjustable for streamwise pressure gradient control and slotted for probe access.

In the present experiments, the two sides of the mixing layer were set to 15 m/s and 9 m/s for a velocity ratio, $r = U_2/U_1 = 0.6$ [$\lambda = (U_1 - U_2)/(U_1 + U_2) = 0.25$]. For these operating conditions, the measured streamwise turbulence level (u'/U_e) was approximately 0.15% and the transverse levels (v'/U_e and w'/U_e) were approximately 0.05%. The mean core-flow was found to be uniform to within 0.5% and cross-flow angles were less than 0.25° (Bell & Mehta 1989a). The boundary layers on the splitter plate were laminar at these operating conditions.

Measurements were made using two independently traversed cross-wire probes. The probes could be rotated in order to measure flow in two-coordinate planes. The geometry of the instrumentation resulted in a minimum probe spacing of 7 mm. One probe was mounted on a 2-D traverse which was designed and constructed for the current work. The new traverse was manually controlled using an indexing stepper motor controller. The second probe was mounted on a pre-existing computer-controlled 3-D traverse. Both cross-wires were linked to a fully automated data acquisition and reduction system controlled by a *DEC MicroVax II* computer. The software required for multiple-probe measurements was developed for the current study. The *Dantec* cross-wire probes (Model 55P51) consisted of 5 μm platinum-plated tungsten sensing elements approximately 1 mm long with

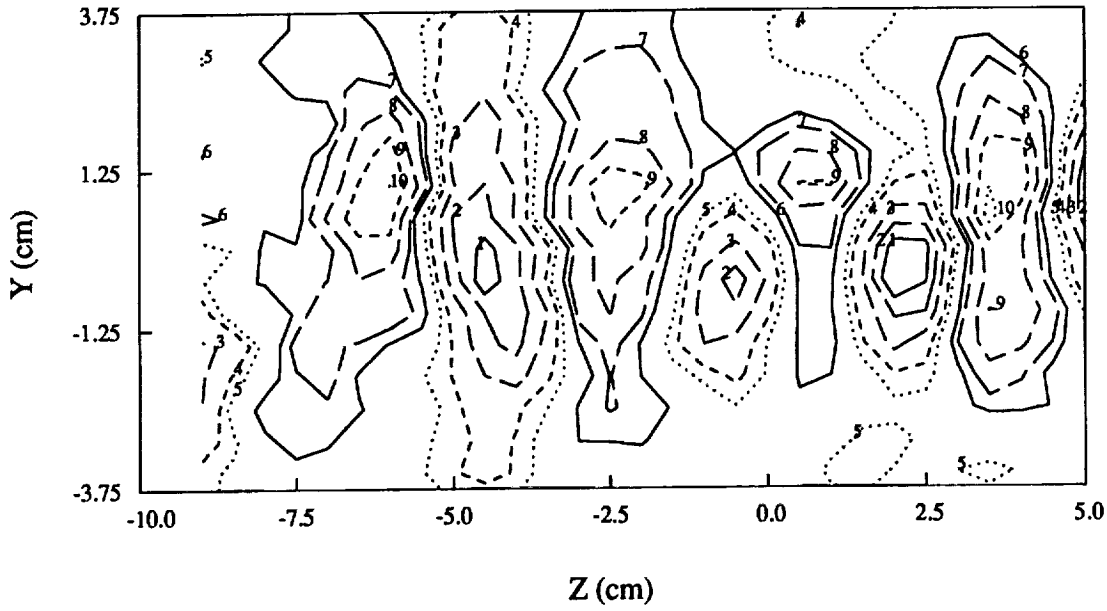

FIGURE 1. Mean streamwise vorticity (Ω_X) at X = 57 cm, starting from -0.08, incremented 0.02.

approximately 1 mm spacing. The probes were calibrated statically in the potential core of the flow assuming a 'cosine-law' response to yaw, with the effective angle determined by calibration. The calibration locations were selected to insure consistent angularity of the measurements of the two probes. The analog signals generated by NASA-built anemometers were DC offset and amplified (x 8) before being fed into a computer interface. The interface contained a fast sample-and-hold A/D converter with 16 bit resolution and a multiplexer for connection to the computer (Bell & Mehta 1992). Individual statistics were averaged over 8192 samples obtained at a rate of 1500 samples per second.

Data were obtained in several Y-Z planes between X = 17 and X = 128 cm with two orientations of the probe (uv and uw) in order to identify mean vortex locations. This method yielded all three components of mean velocity, five independent components of the Reynolds stress tensor, and selected higher order products. Typically, 700-1200 points were measured on a rectangular cross-plane grid at a given streamwise station. The grid spacing (same in both directions, Y and Z) was varied from 0.25-0.5 cm for upstream to downstream stations. The mean spanwise velocity (W) measurements were corrected for mean streamwise velocity gradient ($\partial U/\partial Y$) effects (see Bell and Mehta 1989b for details). The streamwise component of mean vorticity was computed using a central difference numerical differention of the measurements of the velocity components V and W.

An example of the resulting measurement of the mean streamwise vorticity (Ω_X) at X = 57 cm downstream of the splitter plate trailing edge is given in Fig. 1. The

selection of the traverse grid for the correlation measurements is also noted on the figure. Except for the decreasing peak magnitude and increasing size (for increasing streamwise distance), the nominally linear array of counter-rotating vortices was typical of all measurement locations except the first. At the first measurement location, $X = 17$, the streamwise vorticity had not yet organized into a single spanwise row. The correlation locations were nominally selected to cross the location of maximum mean streamwise vorticity.

The two-point cross-correlation measurements required for the estimation of velocity profiles were acquired on grids of equally spaced probe positions. The spacing of measurement locations in the grids was 0.4 cm. The minimum distance between estimation and reference locations was limited by probe geometry to two grid spacings (i.e. 0.8 cm). Therefore, the estimated velocity profile is twice as dense as it could be using probes of the same geometry to measure at all grid locations simultaneously. The grids were positioned 78 cm downstream of the splitter plate trailing edge for the measurements discussed in this paper. It is estimated that this station is located after the third pairing of the spanwise vortex structures.

2.2 Results and discussion

The transverse (v) and spanwise (w) velocity correlations in the spanwise (Z) and transverse (Y) directions, respectively, are shown in Figs. 2a and b for the streamwise location $X = 57$ cm from the splitter plate trailing edge. One noteworthy feature of the sets of curves for each station is the relative phase of each curve. There is generally a shift of the curves from right to left with increasing stationary probe location. There would be a one-to-one correspondence between the change in the probe spacing at the correlation extremes and the change in position of the stationary probe if no meander of the large scale structure is occurring. The transverse velocity correlations on a spanwise measurement grid approximate this no-meander relative phase shift. For example, Figs. 3a and 3b show the probe separation at the first minimum and first maximum (excluding zero spacing) of all of the correlation measurements versus stationary probe location. The slope of the resulting curves for the transverse velocity measurements (Fig. 3a) is very close to -1, indicating that meander in the spanwise (z) direction is negligible at this streamwise location.

The spanwise velocity correlations across the mixing layer have a less consistent phase shift for changing stationary probe location. Typically, the shift of the first minimum is a fraction of the shift of the stationary probe for two sets of correlations (see Fig. 2b). This is reflected in Fig. 3b where the slope of the curve of first minimum versus stationary probe location for the spanwise velocity measurements has a much more gradual slope, which would indicate a large degree of apparent transverse meander. The slope of the curves may be linked to the aspect ratio of the mean streamwise vortices.

A simple, more direct way to identify meander of the large-scale structure is to track them in temporal multi-point velocity records. The presence of streamwise structure should appear clearly in profiles of the secondary velocity. In particular, spanwise meander should produce a jittered signature in spanwise profiles of

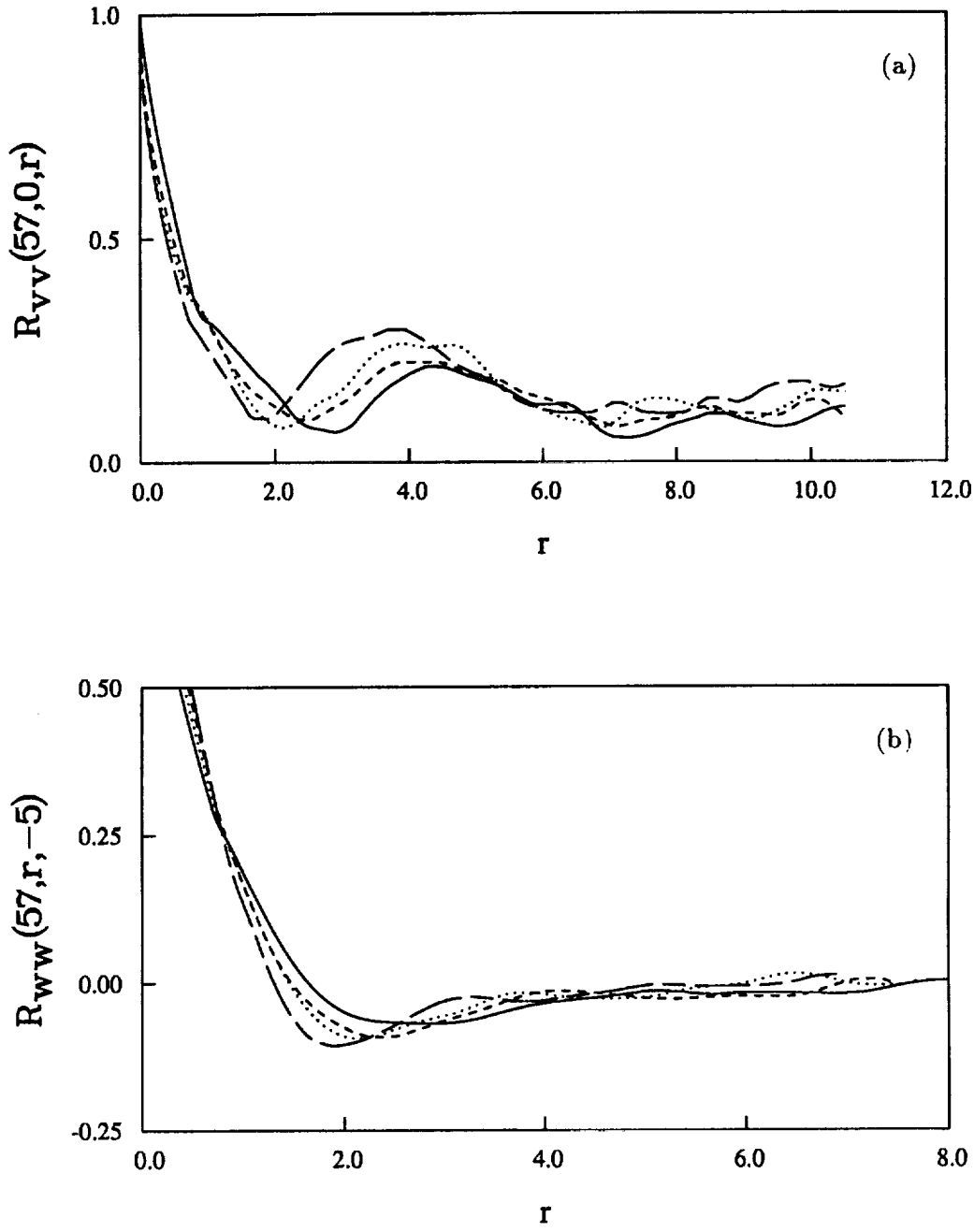

FIGURE 2. Two-point cross-correlation at X = 57 cm. *(a)* Transverse velocity (v) in the spanwise (Z) direction at Y = 0 and Z = -8.5 cm ——— ; -8.15 cm - - - - ; -7.8 cm ····· ; -7.45 cm — — . *(b)* Spanwise velocity (w) in the transverse (Y) direction at Z = -5 cm and Y = -2.1 cm ——— ; -1.4 cm - - - - ; -0.7 cm ····· , 0.0 cm — — .

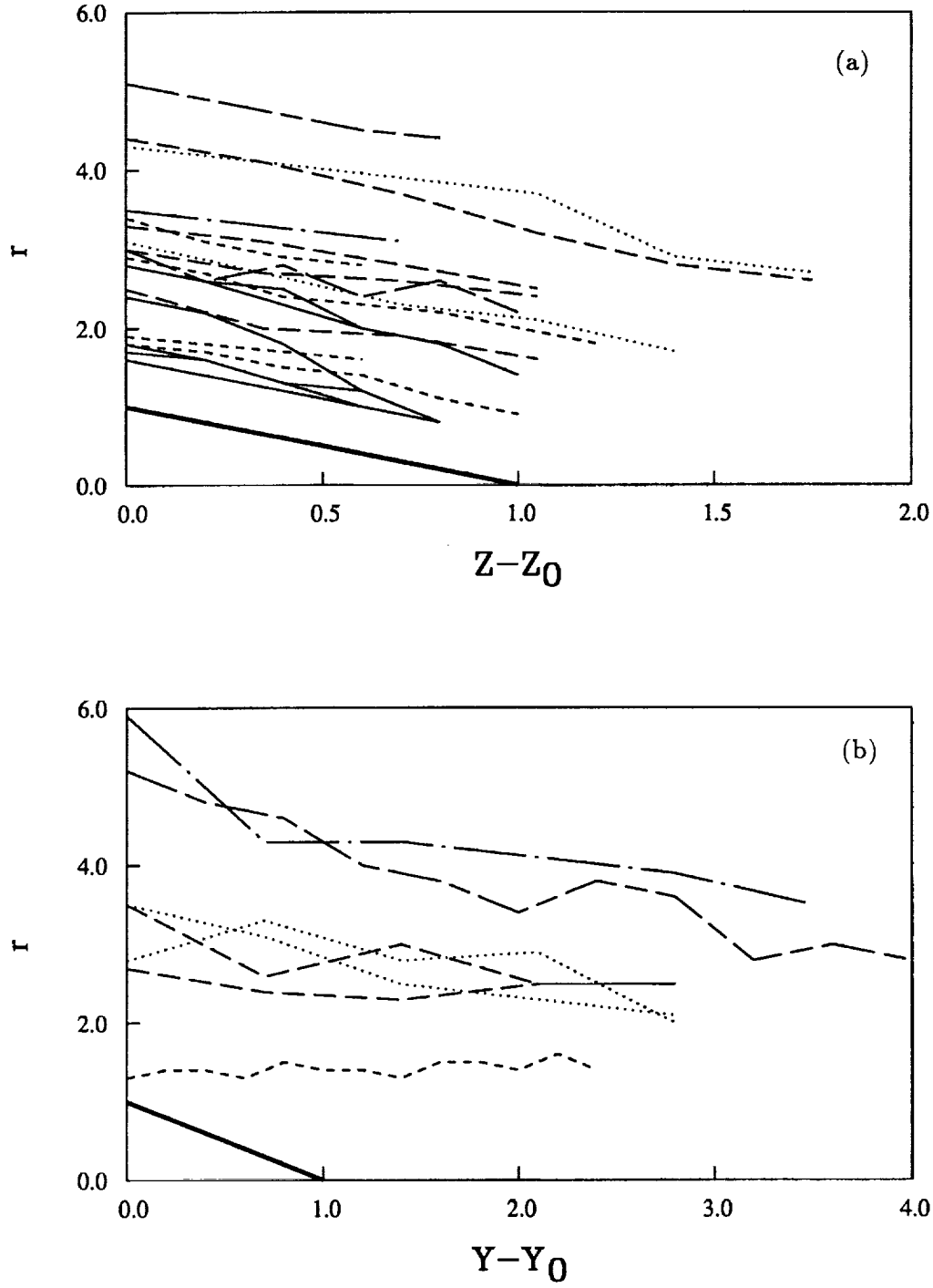

FIGURE 3. Probe separation at extremes of correlations versus relative stationary probe location for X = 27 cm ——— ; 47 cm - - - - ; 57 cm ····· ; 78 cm — — — ; 88 cm ——— ; 128 cm —·— ; Line with slope equal to -1 ———. *(a)* Transverse velocity (v) in the spanwise (Z) direction. *(b)* Spanwise velocity (w) in the transverse (Y) direction.

transverse velocity and transverse meander should produce a jittered signature in transverse profiles of spanwise velocity. Profiles of simultaneous velocity records with sufficient spatial resolution would be very difficult using cross-wire probes and would entail a significant increase in hardware costs. Use of optical techniques such as digital particle image velocimetry would probably be the best suited to this problem, but would also be costly. An alternative approach whereby the velocity profiles were estimated using one or two reference velocities was used to produce simultaneous velocity profiles. This approach required no further investment in hardware.

The linear estimate of the velocity component $\hat{u}_i(x')$ based on m reference (measured) velocity components $u_j(x^{(k)})$ at n locations at the same time can be expressed as:

$$\hat{u}_i(x') = \sum_{k=1}^{n} \sum_{j=1}^{m} A_{ijk} u_j(x^{(k)}). \tag{1}$$

Minimizing the mean-square error, $\overline{[\hat{u}_i(x') - u_i(x')]^2}$, of the estimate yields an equation for the linear estimation coefficients (A_{ijk}):

$$\sum_{k=1}^{n} \sum_{j=1}^{m} A_{ijk} \overline{u_j(x^{(k)}) u_l(x^{(p)})} = \overline{u_l(x^{(p)}) u_i(x')}. \tag{2}$$

Thus, given the cross-correlation tensors, the linear mean-square (MS) estimation coefficients can be determined. It can be shown [using Eq. (1)] that the left hand side of Eq. (2) is equal to $\overline{u_l(x^{(p)}) \hat{u}_i(x')}$. Hence, the estimation-reference cross-correlation tensor is equal to the measurements used to produce the coefficients.

The mean-squared estimation error increases with the distance away from the measurement location (approaching $\overline{u_j^2}$), as the velocity loses correlation with the reference (Adrian & Moin 1988). The estimated signal can be amplified in a rational manner by including the velocity covariance at the estimation locations in the scheme to calculate the estimation coefficients. This optimization which includes the estimation covariance in addition to the two-point cross-correlation tensors forms the basis for the proposed technique.

Consider the error vector,

$$F = \begin{pmatrix} \overline{u_j(x') u_i(x^{(k)})} - \overline{\hat{u}_j(x') u_i(x^{(k)})} \\ \overline{u_j(x') u_i(x')} - \overline{\hat{u}_j(x') \hat{u}_i(x')} \end{pmatrix} \forall i, j, k. \tag{3}$$

Then the estimation coefficients (A_{ijk}) can be optimally determined with respect to both the estimation-reference cross-correlation, $\overline{\hat{u}_j(x') u_i(x^{(k)})}$, and the estimation covariance, $\overline{\hat{u}_j(x') \hat{u}_i(x')}$, by minimizing ($F^T F$), where the superscript T indicates transpose. The statistics of the estimates can be calculated for any value of the coefficients using known reference signals and estimation signals generated using Eq. (1). This optimization can be accelerated, however, by calculating the statistics of the estimates in terms of the reference cross-correlation tensor, $\overline{u_j(x^{(k)}) u_l(x^{(p)})}$,

and the estimation-reference cross-correlation tensor, $\overline{u_l(x^{(p)})u_i(x')}$. By operating on Eq. (1), it can easily be shown that the estimation-reference correlation can be expressed as:

$$\overline{\hat{u}_j(x')u_i(x^{(k)})} = \sum_{p=1}^{n}\sum_{q=1}^{m} A_{jqp}\overline{u_q(x^{(p)})u_i(x^{(k)})} \tag{4}$$

and the estimated Reynolds stresses can be expressed as:

$$\overline{\hat{u}_j(x')\hat{u}_i(x')} = \sum_{p=1}^{n}\sum_{q=1}^{m}\sum_{k=1}^{n}\sum_{l=1}^{m} A_{jqp}A_{ilk}\overline{u_q(x^{(p)})u_l(x^{(k)})}. \tag{5}$$

Thus, the new technique requires the same cross-correlation tensor data as the traditional mean-square estimate along with the estimation covariance data. The optimization described above is a non-linear, least-squares optimization which can be solved using standard techniques such as, for example, the modified Levenberg-Marquardt algorithm implemented in the *IMSL* subroutine DUNLSF.

Another alternative to minimizing the mean-squared error is to maximize the correlation coefficient of the estimated signal and the true signal at the estimation location. When this criterion is used to determine the linear estimation coefficients for a two-component one-point estimate, the maximum correlation coefficient is independent of the energy of the estimate:

$$\rho_{ii} = \left(\frac{-\overline{\hat{u}_i^2(x')}a}{(b/2)^2 - \overline{u_1^2(x^{(k)})}\left[\overline{\hat{u}^2(x')}\right]^2 a / \left[\overline{\hat{u}(x')u_1(x^{(k)})}\right]^2} \right)^{1/2} \tag{6}$$

where

$$a = \frac{\left[\overline{\hat{u}(x')u_2(x^{(k)})}\right]^2 \overline{u_1^2(x^{(k)})}}{\left[\overline{\hat{u}(x')u_1(x^{(k)})}\right]^2} + \overline{u_2^2(x^{(k)})} - \frac{2\overline{\hat{u}(x')u_2(x^{(k)})u_1(x^{(k)})u_2(x^{(k)})}}{\overline{\hat{u}(x')u_1(x^{(k)})}} \tag{7}$$

and

$$b = \frac{2\overline{\hat{u}^2(x')}}{\overline{\hat{u}(x')u_1(x^{(k)})}}\overline{u_1(x^{(k)})u_2(x^{(k)})} - \frac{\overline{\hat{u}(x')u_2(x^{(k)})u_1^2(x^{(k)})}}{\overline{\hat{u}(x')u_1(x^{(k)})}}. \tag{8}$$

Hence, once the maximum correlation coefficient has been calculated, the estimation coefficients can then be determined from

$$A_2 = \frac{-\rho_{ii}b}{2a} \tag{9}$$

and

$$A_1 = \frac{\rho_{ii}\overline{\hat{u}^2(x')} - A_2\overline{\hat{u}(x')u_2(x^{(k)})}}{\overline{\hat{u}(x')u_1(x^{(k)})}}, \tag{10}$$

consecutively. This restricts the energy of the estimate to the measured energy at the estimate location.

Verification of the MS estimation and the new estimation schemes outlined above are detailed below. The verifications include comparisons of partial kinetic energy and the estimation-measurement correlation coefficient. Due to the simplicity of the linear estimation, these quantities (and many others) can be calculated using *only* the statistics required for the coefficient calculation (i.e. the time series do not have to be retained). For example, the partial kinetic energy of the estimated velocity signals can be expressed in terms of the Reynolds stresses given by Eq. (5). Similarly, the estimation-measurement correlation coefficient

$$\rho_{ij} = \frac{\overline{\hat{u}_j(x')u_i(x')}}{[\overline{\hat{u}_j^2(x')u_i^2(x')}]^{1/2}} \tag{11}$$

can be expressed in terms of the optimization data, $\overline{u_i^2(x')}$ and $\overline{u_q(x^{(p)})u_i(x^{(k)})}$, since the estimation-measurement correlation is given by:

$$\overline{\hat{u}_j(x')u_i(x')} = \sum_{p=1}^{n}\sum_{q=1}^{m} A_{jqp}\overline{u_q(x^{(p)})u_i(x^{(k)})} \tag{12}$$

and $\overline{\hat{u}_j^2(x')}$ can be obtained from Eq. (5). By not requiring the calculation of such statistics from entire time series, optimum reference locations can quickly be determined without extensive calculation or data storage costs. Furthermore, the appropriate number of references to be used for time-series estimation can be selected using *only* two-point measurements.

Cole *et al.* (1992) suggested comparison of the partial kinetic energy $(\overline{u_1^2} + \overline{u_2^2})$ in order to quantify the effectiveness of the estimation. The results of such a comparison for two sets of reference locations are shown in Figs. 4a and b. Note that in all figures, the results of the estimation schemes have been designated MS for the traditional mean-square estimate, LS for the new technique requiring the non-linear least-squares fit, and OP for the new technique which maximizes the estimation-measurement correlation coefficient. By taking two reference locations near the center of the mixing layer (Fig. 4a), the traditional stochastic estimate appears to recover a large fraction of the measured energy. This result is consistent with the findings for the jet mixing layer (Cole *et al.* 1992). Unfortunately, most of the energy contribution is from the references and little energy is represented by the estimates. It may also be noted in Fig. 4a that including the estimation covariance to the optimization for this choice of reference locations improves the energy recovery of the estimate very little ($\sim 10\%$). The result of taking reference locations near the edges of the mixing layer is shown in Fig. 4b. The traditional stochastic estimate for these choices of reference locations yield a negligible representation of the energy away from those locations. The estimation proposed here gave a very good representation of the energy; even better than that obtained for more centrally located references (as in Fig. 4a). The reason for the large improvement over mean-square

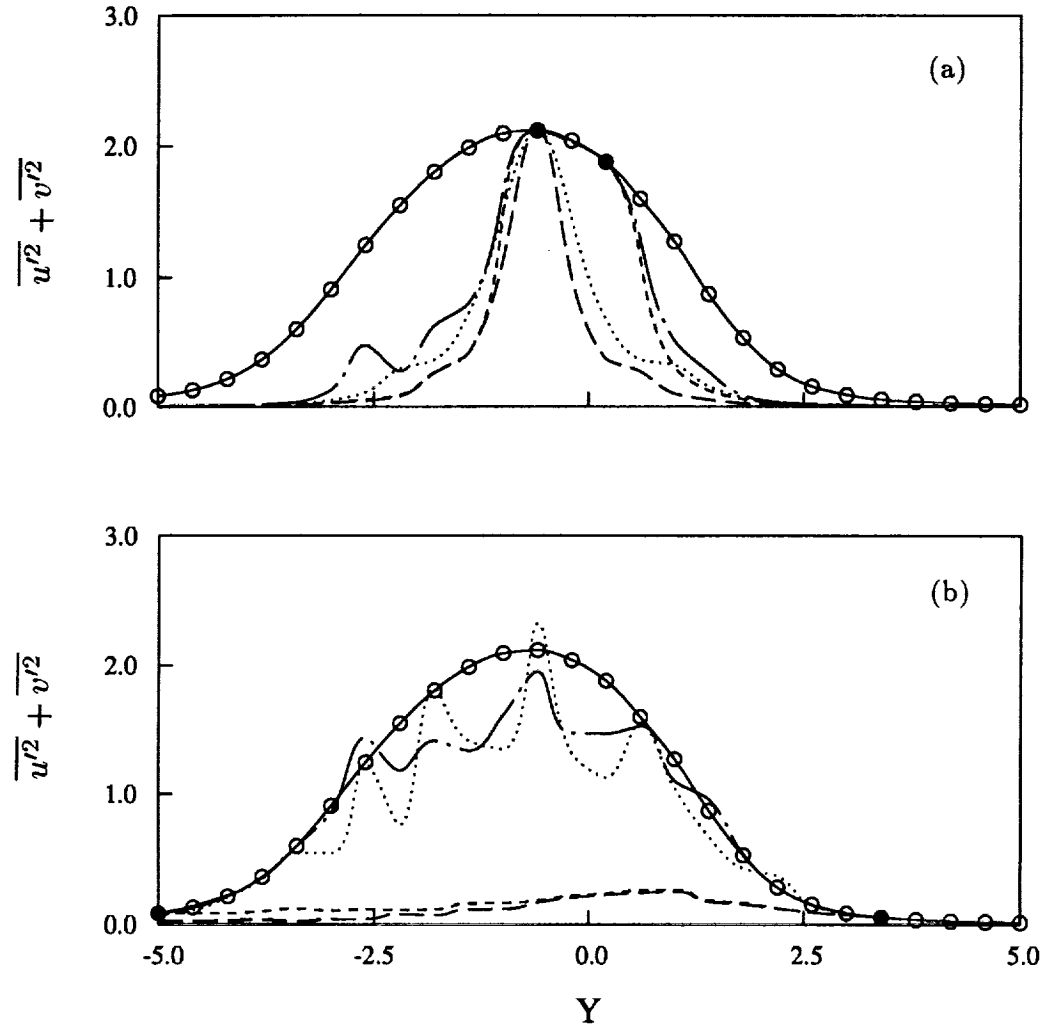

FIGURE 4. Transverse partial kinetic energy comparisons. *(a)* Two-point estimates with references at Y = -0.6 cm and Y = 0.2 cm and one-point estimates with reference at Y = -0.6 cm. *(b)* Two-point estimates with references at Y = -5.0 cm and Y = 3.4 cm and one-point estimates with reference at Y = 3.4 cm, Measured o ; Measured reference • ; Two-point MS ---- ; Two point LS —·— ; One-point MS ——— ; One-point LS ····· ; One-point OP ——— .

estimation for this choice of reference locations is that the estimate-reference cross-correlation is much less than the estimation covariance. Therefore, minimizing the error in both quantities results in a better fit to the estimation covariance (which includes $\overline{u_1^2}$ and $\overline{u_2^2}$). This trade-off does not occur for reference locations near the center of the mixing layer. Consequently, the energy recovery for spanwise profiles

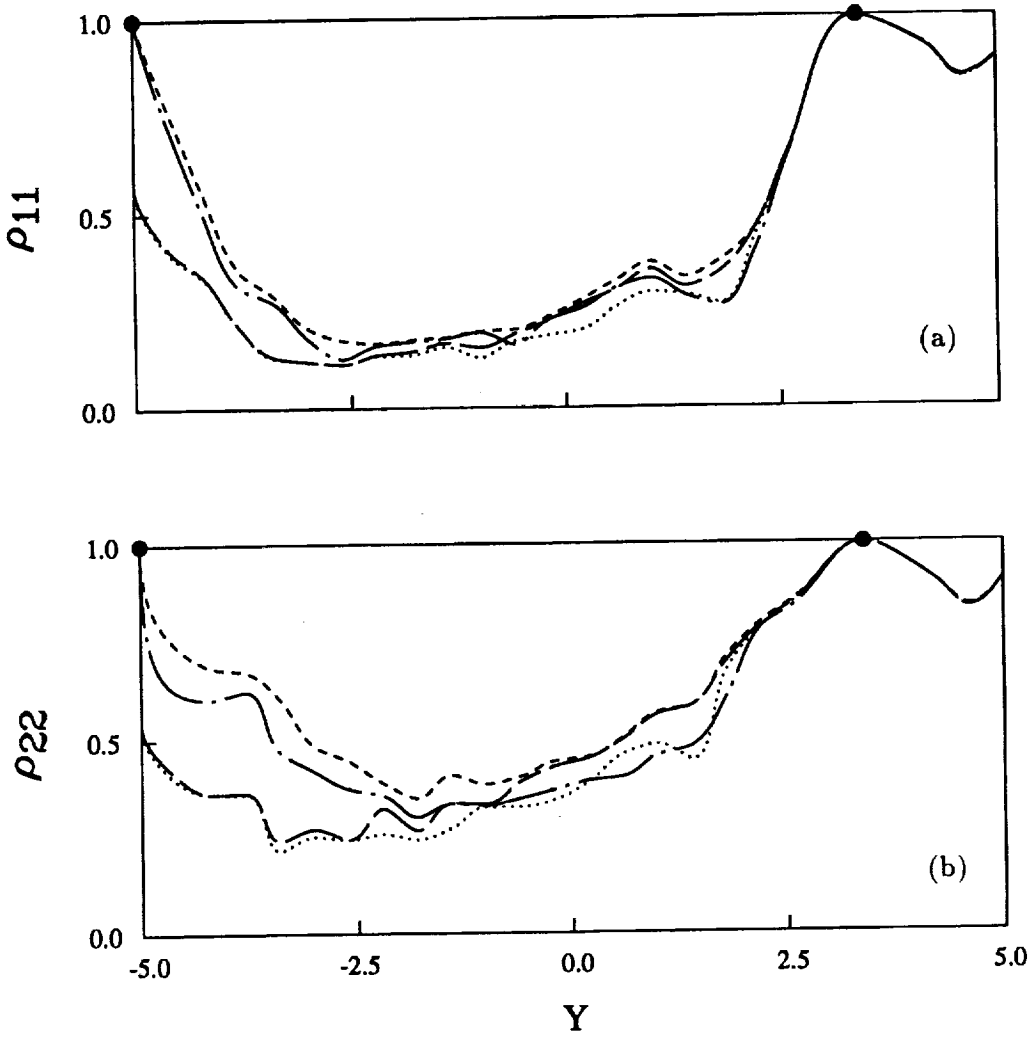

FIGURE 5. Transverse estimation-measurement correlation coefficients. Two-point estimates with references at Y = -5.0 cm and Y = 3.4 cm and one-point estimates with reference at Y = 3.4 cm. *(a)* Streamwise component (u). *(b)* Transverse component (v), Reference • ; Two-point MS ---- ; Two-point LS —·— ; One-point MS — — — ; One-point LS ····· ; One-point OP —— — .

near the center of the mixing layer was very poor for both estimation techniques. By taking spanwise grids near the mixing layer edge, a very good representation of the energy by the new estimation was obtained.

Another measure of the success of an estimation is the correlation coefficient for corresponding estimated and measured velocities at the same location. If an estimated velocity matches the measurement exactly, then the correlation coefficient

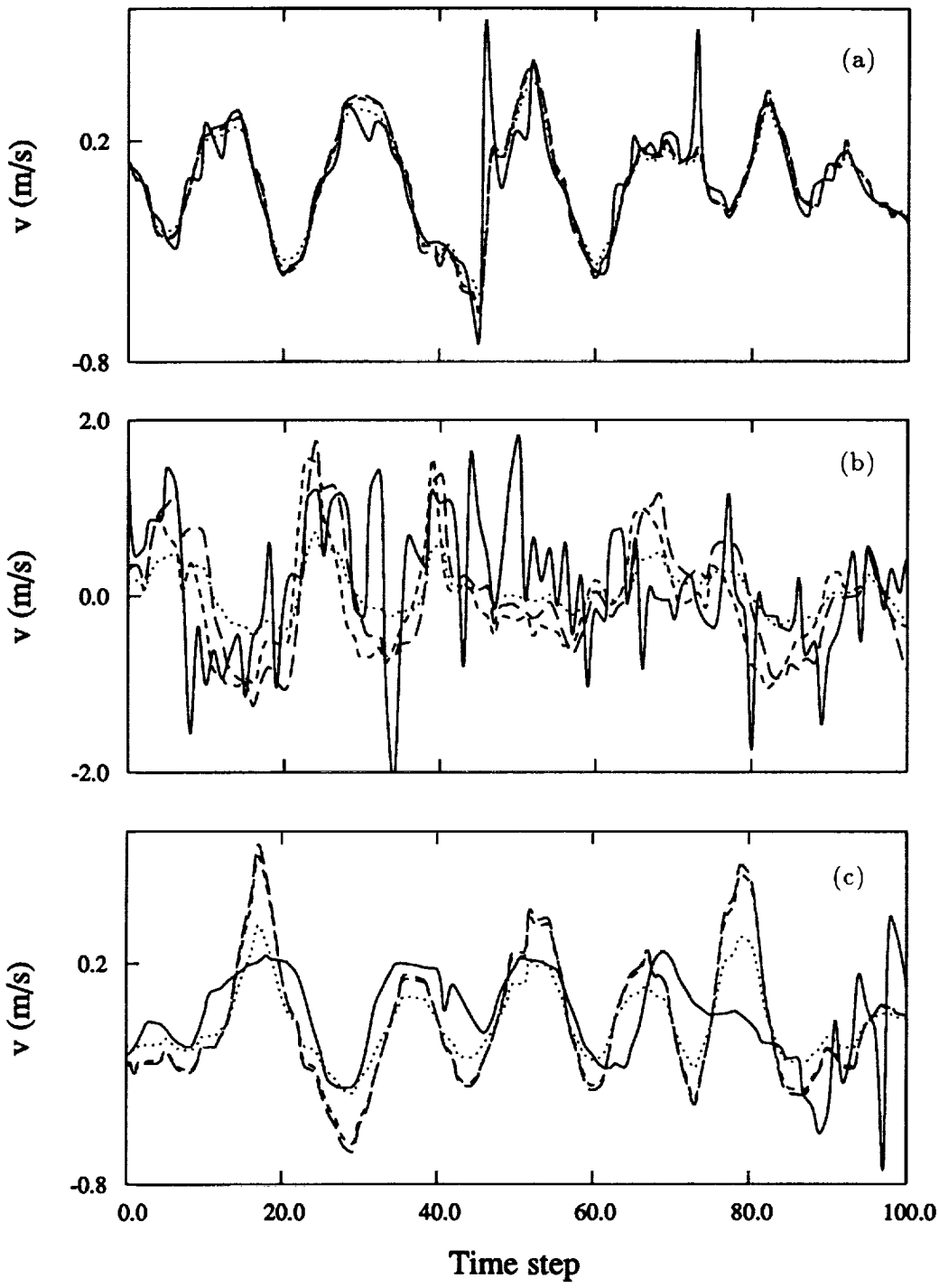

FIGURE 6. Transverse velocity (v) measurement vs. estimate time series comparisons for a reference at Y = 3.4 cm. *(a)* Y = 2.6 cm. *(b)* Y = -0.6 cm. *(c)* Y = -5.0 cm, Measured ——— ; MS ····· ; LS - - - - ; OP — — — .

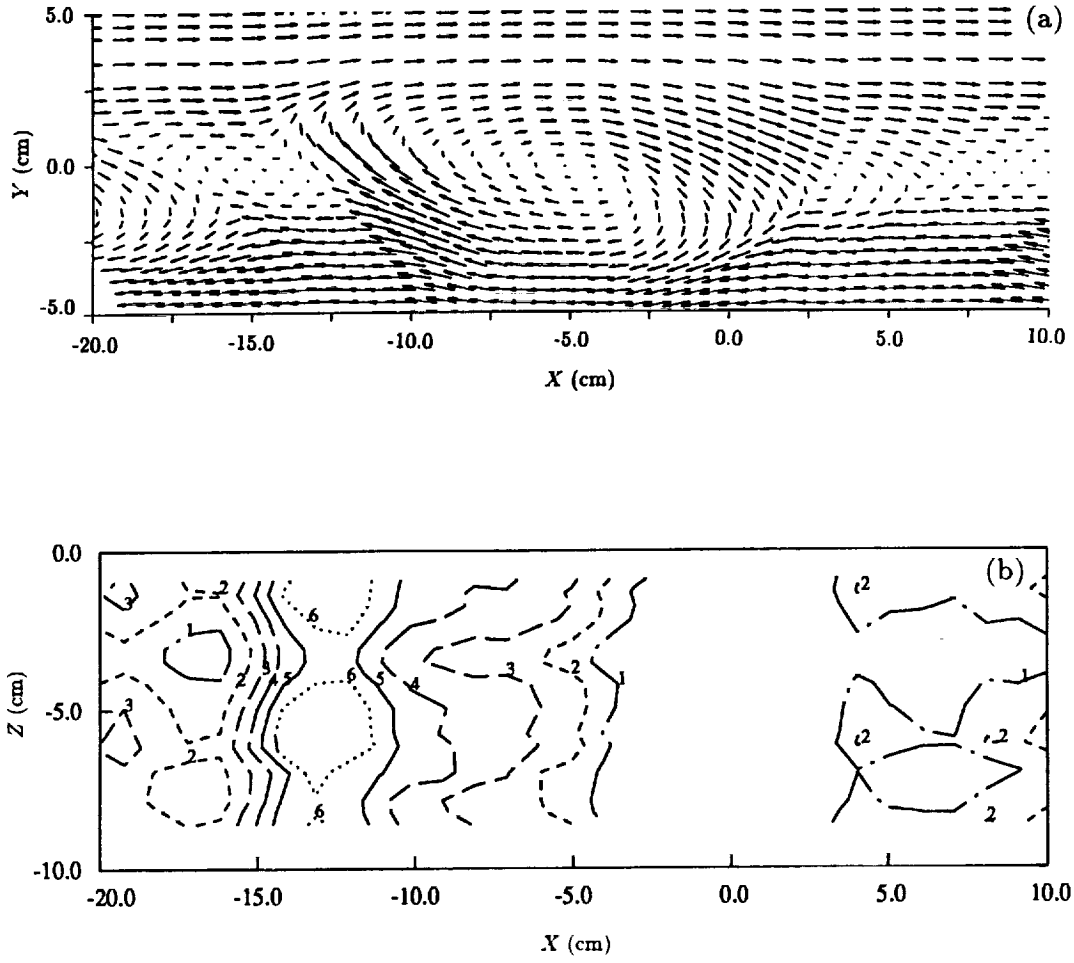

FIGURE 7. Estimated velocity profiles. *(a)* Transverse secondary velocity vectors at Z = -7.0 cm for a reference at Y = -3.4 cm. *(b)* Spanwise profile of transverse velocity at Y = 3.4 cm for references at Z = -5.0 cm and Z = -7.0 cm, starting from -0.1 m/s, incremented 0.08 m/s.

would obviously be equal to one. The results of a calculation of the correlation coefficient for a high speed edge reference are shown in Figs. 5a and b. A high correlation between the estimation and corresponding measurement exists for most of the high-speed side locations. This is reflected in the corresponding time trace comparisons of Fig. 6a. It is no surprise that the low frequency trigger provided by the flow near the mixing layer edge does not yield estimates which are highly correlated with the high frequency signals near the mixing layer center (see Fig. 6b). The low frequency estimate resulting from the technique proposed here is largely an amplified version of the MS estimate. The amplification is a result of an attempt (by the optimization) to match the covariance of the estimate to that of the measured

signal. The estimation of flow on the opposite side of the layer is remarkably good as suggested by the high correlation coefficient for those locations (Figs 5a and b). Presumably, the large-scale structure providing the trigger at the high-speed edge produces similar signatures at the low speed edge, resulting in a good estimation of the flow there (Fig. 6c). The streamwise component time series comparisons were left out for brevity since they were qualitatively similar to the transverse component comparisons of Figs. 6a through 6c.

The results of estimating the one-component simultaneous multi-point velocity profile using the OP method is presented as Fig. 7a. This profile was generated for a transverse grid at Z = -7 cm using a reference at Y = -5 cm. Taylor's hypothesis was used to approximate the spatial development from the temporal signals. This entailed calculating the relative spatial locations of velocity vectors as U_c/fs, where f_s is the sampling frequency and U_c is the mean convection velocity. The secondary velocity vector plot clearly shows the spanwise rollers passing through the measurement station. In spite of the poor representation of the broad-band signals near the center of the mixing layer, the large-scale structure is adequately represented when edge references are selected. In particular, the relationship between the kinematics of the large-scale streamwise and spanwise flow structures can be inferred from simultaneous estimates of velocity profiles on spanwise and transverse grids. For example, using two cross-wire probes makes it possible to estimate three velocity components in one profile (in one direction) and two velocity components in another profile (in another direction) provided the grids have a common reference location. This can be achieved by measuring reference signals u_1 and u_2 (or u_3) at the common grid location and simultaneously measuring u_1 u_3 (or u_2) in the grid for which three velocity components are desired. With the use of such a combination of grid locations, it was possible to estimate the transverse velocity (v) as shown in Fig. 7b. The signature of the streamwise vortices which ride the braid between spanwise vortices appear each time the spanwise vortices carry them through the measurement grid. This gives rise to the juxtaposed spanwise sets of islands in Fig. 7b between time steps -17 and -12. The lack of significant structure to structure spanwise relative motion of this signature observed in longer simultaneous time series profiles is indicative of the low degree of spanwise meander which was also inferred from the correlation measurements.

3. Future plans

During the remainder of the program, phase locked velocity measurements will be obtained by acoustically forcing the mixing layer. The hardware required for this phase of the program has already been prepared. By establishing a periodic sequence of spanwise vortices, it should be possible to examine the detailed structure of the streamwise vortices. By measuring the scale and spacing of the streamwise vorticity in the braid region of the mixing layer vortices, more direct comparisons of the wind tunnel measurements can be made with the direct numerical simulations of the same flow (Rogers, M. M. & Moser, R. D. private communication). In particular, initial conditions (streamwise vortex strength and distribution) will be measured in detail so that they may be used as input to numerical simulations.

During the latter part of the program, some scalar mixing studies using heat to tag one of the streams will also be conducted. An extension of the estimation to include space-time correlations will also be attempted if time permits.

Acknowledgements

This work is being performed in the Fluid Mechanics Laboratory, NASA Ames Research Center in collaboration with Dr. R. D. Mehta.

REFERENCES

ADRIAN R. J. & MOIN, P. 1988 Stochastic estimation of organized turbulent structure: homogeneous shear flow. *J. Fluid Mech.* **190,** 531.

BELL, J. H. 1990 An Experimental Study of Secondary Vortex Structure in Mixing Layers. *Annual Research Briefs.* Center for Turbulence Research, Stanford Univ./NASA Ames, 59-79.

BELL, J. H. & MEHTA, R. D. 1989a Design and Calibration of the Mixing Layer Wind Tunnel. *JIAA TR-84.* Dept. of Aeronautics and Astronautics, Stanford University.

BELL, J. H. & MEHTA, R. D. 1989b Three-Dimensional Structure of Plane Mixing Layers. *JIAA Report TR-90.*

BELL, J. H. & MEHTA, R. D. 1990 Development of a Two-Stream Mixing Layer from Tripped and Untripped Boundary Layers. *AIAA Journal.* **28,** 2034-2042.

BELL, J.H. AND MEHTA, R.D. 1992 Measurements of the Streamwise Vortical Structures in a Plane Mixing Layer. *J. Fluid Mech.* **239,** 213.

BERNAL, L. P. & ROSHKO, A. 1986 Streamwise Vortex Structure in Plane Mixing Layers. *J. Fluid Mech.* **170,** 499-525.

COLE, D. R., GLAUSER, M. N. & GUEZENNEC, Y. G. 1992 An application of the stochastic estimation to the jet mixing layer. *Phys. Fluids A.* **4,** 192.

LEBOEUF, R. L. & MEHTA, R. D. 1992 An Improved Linear Estimation Scheme. *Bulletin of American Physical Society, Division of Fluid Dynamics, 45th Meeting.* also submitted to *Phys. Fluids A.*

TOWNSEND, A. A. 1976 *Structure of Turbulent Shear Flow* (2nd Edition) Cambridge University Press.